

Galaxy Distances via Rotational Parallaxes

Rob P. Olling

Rutgers University, NJ

and

D. M. Peterson

SUNY at Stony Brook, NY

ABSTRACT

Astrometry is one of the foundations of astrophysics. Accurate distances to stars and galaxies allow for significant tests of stellar evolution, galaxy formation and evolution and cosmology. NASA's Space Interferometry Mission (SIM) will obtain extraordinary precision astrometry [1-10 μ as positional accuracy] for ten to twenty thousand objects brighter than $V=20$ mag. In this paper we discuss a method to determine the distance of nearby spiral galaxies using the technique of rotational parallaxes. We show that it is possible to achieve distance errors of only a few percent using this method. With such distances at hand, it becomes possible to determine an accurate zero-point for the Tully-Fisher relation, one of the tools to measure distances throughout the universe. Precision cosmology will become possible once the Hubble constant has been accurately determined from a SIM-based calibration of the Tully-Fisher relation. The rotational parallax method employs the common motions of a number of stars to determine the distance to the group as a whole. If we assume that a given target star in an external galaxy is on a circular orbit around the center of that galaxy, three observables—the two proper motions and the radial velocity—suffice to determine the three unknowns: the inclination of the orbit, the rotational velocity and the distance. Several factors complicate the application of this simple technique to real galaxies: 1) the target galaxy may have substantial space-motion, 2) stars in real galaxies are not on circular orbits (e.g. due to spiral-arm streaming motions or induced by random motions), 3) stars in the galaxy are at significantly different distances from the Sun (the near side of M 31 is $\sim 5\%$ closer than the far side), 4) target stars might have large z -heights or velocities (“run-away” stars). In this paper we show how one-percent distances can be obtained for the nearest spirals, even in the presence of the complications mentioned above.

1. Introduction

At the moment, astrometry is undergoing a quiet revolution. ESA's Hipparcos mission set the stage. Currently there are two Hipparcos++ missions in preparation: USNO leads a collaboration to build FAME¹, a MIDEEX type mission to be launched in 2004, and Germany is planning the DIVA² mission. These spacecraft will extend the reach of astrometry to about two kpc from 100 parsec. Space interferometry is the next step, with the ultimate goal to detect and characterize Earth-like planets around nearby stars (NASA's TPF and ESA's DARWIN missions). Before that, NASA's Space Interferometry Mission (SIM) can determine the distances to virtually any star in the Milky Way with an accuracy of a few percent. Many important problems in Milky Way research can be solved with micro-arcsecond astrometric data.

SIM will also contribute significantly to the field of cosmology. Globular clusters play an important role in cosmology in that they contain the oldest stars known to mankind. However, precise age determinations are currently hampered by the lack of accurate distances. SIM will provide such distances, and will hence establish a firm lower limit to the age of the universe. SIM would contribute more directly to cosmology if its data could be used to establish the parallax of nearby spirals and hence provide a calibration of the zero-point of the Tully-Fisher (TF) relation. The Tully-Fisher relation is one of the tools to measure the expansion rate (H_0) of the universe. A SIM-based determination of the zero-point of the TF relation would thus directly yield a determination of H_0 with an accuracy of several percent, an order of magnitude improvement over the current state of affairs.

Unfortunately, SIM's phenomenal precision is still not quite good enough to achieve this. However, other, only slightly less direct methods can be applied. In this paper we describe one of those techniques: the rotational parallax method.

2. The Rotational Parallax Method: The Circular Orbit Case

Imagine a nearby spiral galaxy at distance, D (in Mpc), inclined with respect to the line of sight (by i degrees) that has a rotational speed of V_c km s⁻¹. The Andromeda galaxy (M 31, NGC 204) is such a galaxy ($D \sim 0.77, i \sim 77^\circ$). Its rotational speed ($V_c \sim 270$) induces a proper motion of $\mu = \frac{V_c}{\kappa D} \sim 73.9 \mu\text{as yr}^{-1}$. Here κ is a constant that arises from the choice of units, and $\kappa \sim 4.74$ if D is measured in Mpc and μ in micro-arcsec per year.

¹<http://aa.usno.navy.mil/fame/>

²<http://www.aip.de/groups/DIVA/>

Such proper motion is easily resolvable with an instrument such as SIM.

In Fig. 1 we present a sketch of how a typical nearby spiral might appear on the sky (bottom panel). In the plane of the galaxy (top panel) we use two coordinate systems: rectangular (x and y) and polar (R and θ). Projected on the plane of the sky, the x and y' coordinates axes coincide with the major and minor axes, respectively. The y' coordinate is the foreshortened y coordinate.

In this section we will discuss the simplified case that all stellar orbits are circular, more realistic situations are discussed in § 4. The following elementary relations between the coordinates and the various projections of the orbital speed \overline{V}_c are derived with the aid of Fig. 1:

$$x = R \cos \theta \quad (1)$$

$$y = R \sin \theta \quad (2)$$

$$y' = \frac{y}{\cos i} = \frac{R \sin \theta}{\cos i} \quad (3)$$

$$\tan \theta = \frac{y}{x} = \frac{y'}{x \cos i} \quad (4)$$

$$V_x = -s_\Omega V_c \sin \theta' \quad (5)$$

$$V_y = s_\Omega V_c \cos \theta' = -\frac{V_x}{\tan \theta'} \quad (6)$$

$$V_r = V_y \sin i \quad (7)$$

$$V_{y'} = V_y \cos i = \kappa \mu_{y'} D \quad (8)$$

$$V_x = \kappa \mu_x D \quad (9)$$

$$\cos \theta' = \frac{V_y}{\sqrt{V_x^2 + V_y^2}} = \frac{\mu_{y'}}{\sqrt{\mu_{y'}^2 + \mu_x^2 \cos^2 i}} \quad (10)$$

where V_x and V_y are the projections of \overline{V}_c on the x and y axes. The angle θ' between \overline{V}_c and V_y equals $\theta \equiv \arctan(y/x)$ for circular orbits. V_r is the radial velocity along the line of sight and V_x and $V_{y'}$ are the components of \overline{V}_c along the apparent major and minor axes. The requirement that velocities are positive in the $+x$ and $+y$ directions leads to $s_\Omega = +1$ for counter-clockwise rotation, and $s_\Omega = -1$ for clockwise motions. The observable proper motions along x and y' are symbolized by μ_x and $\mu_{y'}$, respectively.

2.1. The Principal Axes Method

The derivation of distances from observed proper motions and radial velocities is a well established practice in astronomy (e.g. orbital parallax), and are among the most reliable

distance measures available. Since the proper motion is the ratio of a velocity (in km s^{-1}) and the distance, the latter can be determined from observations. A common problem is that the angle between the space velocity and the line-of-sight is typically not known, so that the distance is determined modulo $\tan i$. For external galaxies, the inclination is well established from the axis ratio of the image and/or from the analysis of H I or H α radial velocity fields.

The principal axis method is particularly appealing for the case of circular orbits³. For elliptical orbits we have to introduce two additional a priori unknown angles: the angle $\Delta\theta_M$ between the orbital velocity (\overline{V}_o) and the tangent to a circular orbit at the major axis, and the angle between a circular and an elliptical orbit at the minor axis, $\Delta\theta_m$. These two angular differences are related to the eccentricity (e) and position angle (ϕ) of the elliptical orbit. Before proceeding in the derivation of the distance, it is profitable to re-write equations (7)-(9) for stars located on the principal axes:

$$\begin{aligned}
 V_{r,M} &= V_r(\cos\theta = \pm 1) = V_y \sin i = s_\Omega V_o \cos \Delta\theta_M \sin i \\
 \mu_M &= \mu_{y'}(\cos\theta = \pm 1) = \frac{V_{y'}}{\kappa D} = s_\Omega \frac{V_o \cos \Delta\theta_M \cos i}{\kappa D} \\
 \tan \Delta\theta_M &= \frac{\mu_x(\cos\theta = \pm 1)}{\mu_{y'}(\cos\theta = \pm 1)} \\
 \mu_m &= \mu_x(\sin(\theta) = \pm 1) = \frac{V_x}{\kappa D} = -s_\Omega \frac{V_o \cos \Delta\theta_m}{\kappa D},
 \end{aligned} \tag{11}$$

where $V_{r,M}$ and μ_M are the radial and proper motion on the major axis and μ_m equals the proper motion on the minor axis. With an assumed inclination the first two equations of (11) can be solved for the “major-axis” distance D_M [eqn. (12) below]. Further simplifications can be made in case the orbits are circular, so that the $\cos \Delta\theta_M$ and $\cos \Delta\theta_m$ terms in (11) equal unity. D_M and the “minor-major axes” inclination and distance are given by:

$$D_M = \frac{V_c \cos i}{\kappa |\mu_M|} = \frac{|V_{r,M}|}{\kappa \tan i |\mu_M|} \tag{12}$$

$$\sin i_{mM} = \sqrt{1 - \frac{\mu_M}{-\mu_m}} \tag{13}$$

$$D_{mM} = \frac{|V_{r,M}|}{\kappa \sqrt{\mu_m^2 - \mu_M^2}}. \tag{14}$$

A clear advantage of the mM method is that the systemic motion of the galaxy as a whole can be taken out easily by considering points symmetric with respect to the center of the galaxy. Rotation-induced proper motions at symmetric points have opposite sign, while the

³We do not consider out-of-the plane components here.

radial and planar components of the systemic velocity (V_{sys}) have the same orientation and magnitude. The rotation-induced proper motion component can thus be easily computed. For example, when taking out the systemic motion, μ_m, μ_M and $V_{r,M}$ in equations (12)-(14) should be replaced by $\mu_m = \frac{1}{2}[\mu'_m(\theta = -90) - \mu'_m(\theta = +90)]$ and similar relations for V_r and μ_M . The primed relations indicate the observed motions that include the projection of the systemic motion.

One potential disadvantage of this principal axes or nM method [cf. eqn. (14)] is that the measurements of μ_m and μ_M are to be taken at the same galactocentric radius, or from radii with the same circular velocity and inclination. In the discussion above we did not consider the possibility that the actual distances to the target stars may differ significantly, which may be the case for the nearest galaxies (up to 5% for M 31 & M 33). However, application of the major-axis method (12) is unaffected by this problem. We present a more general distance solution in later sections.

2.2. The Single Star Method

Another potential disadvantage of the mM method is that the available surface area in the galaxy for suitable stars is relatively small, since the target stars are limited to regions close to the principal axes and because suitably bright targets are quite rare. Fortunately, other rotational parallax varieties exist, and we discuss their merits below.

In fact, we can determine the distance of a single stars if we neglect, for now, the systemic motion of the galaxy and the random motions of the stars. Using some of the relations (1)-(9), we solve for the inclination of the stellar orbit:

$$\cos i = \frac{\mu_{y'}}{-\mu_x} \tan \theta' \quad (15)$$

$$\cos^2 i = \frac{\mu_{y'} y'}{-\mu_x x}, \quad (16)$$

Equation (15) holds for any type of orbit, circular or elliptical. Further, if the orbit is circular we can equate θ and θ' and arrive at equation (16). The orbital speed can be computed from the radial velocity [eqn. (7)]: $V_o = \frac{V_r}{\cos \theta' \sin i}$. This equation can be re-written for the elliptical and circular orbit cases with the aid of eqns. (10) and (16), respectively:

$$V_o = V_r \sqrt{1 + \frac{1}{\tan^2 i}} \left(1 + \frac{\mu_x^2}{\mu_{y'}^2} \right) \quad (17)$$

$$V_c = V_r \sqrt{\frac{\mu_x}{\mu_{y'}} \frac{x\mu_{y'} - y'\mu_x}{x\mu_x + y'\mu_{y'}}} \quad (18)$$

In the last equation we expressed the trigonometric terms in the primary observables.

A rotational parallax distance can now be obtained by combining the radial velocity and either the proper motion perpendicular or parallel to the major axis. As was the case for the principal axis method, we need to make a distinction between the case of elliptical and circular orbits. If the orbit is elliptical, the distance must be calculated from V_r and $\mu_{y'}$, and depends *only* on the assumed inclination. In the circular orbit case the expressions obtained from the μ_x and $\mu_{y'}$ are identical and can be re-written in terms of observable quantities only. For the two single-star distances we find:

$$D_{y'} = \frac{V_r}{\kappa \mu_{y'} \tan i} \quad (19)$$

$$D_{PP} = \frac{V_r}{\kappa} \sqrt{-\frac{y'/\mu_{y'}}{x\mu_x + y'\mu_{y'}}} \quad (20)$$

We will refer to distances calculated from the perpendicular and parallel proper motions of individual stars [eqn.(20)] as “*PP* distances.”

2.3. Error Estimates

It is instructive to estimate the attainable errors using SIM astrometry. This is most easily done for the case of circular orbits. Below we present the expressions for the errors in the inferred distance, inclination and circular velocity, where we express all trigonometric terms in the primary observables:

$$\frac{\Delta D_{y'}}{D_{y'}} = \sqrt{\left(\frac{\Delta V_r}{V_r}\right)^2 + \left(\frac{\Delta \mu_{y'}}{\mu_{y'}}\right)^2} \quad (21)$$

$$\frac{\Delta D_{mM}}{D_{mM}} = \sqrt{\left(\frac{\Delta V_r}{V_r}\right)^2 + \left(\frac{\mu_m \Delta \mu_m}{\mu_m^2 - \mu_M^2}\right)^2 + \left(\frac{\mu_M \Delta \mu_M}{\mu_m^2 - \mu_M^2}\right)^2} \quad (22)$$

$$\frac{\Delta \cos^2 i}{\cos^2 i} = \sqrt{\left(\frac{\Delta \mu_{y'}}{\mu_{y'}}\right)^2 + \left(\frac{\Delta \mu_x}{\mu_x}\right)^2} \quad (23)$$

$$\begin{aligned} \left(\frac{\Delta V_c}{V_c}\right)^2 &= \left(\frac{\Delta V_r}{V_r}\right)^2 + \left(\frac{y' x(\mu_x^2 - \mu_{y'}^2) + 2y' \mu_x \mu_{y'}}{2(x\mu_x + y'\mu_{y'})(x\mu_{y'} - y'\mu_x)}\right)^2 \times \\ &\quad \left(\left(\frac{\Delta \mu_x}{\mu_x}\right)^2 + \left(\frac{\Delta \mu_{y'}}{\mu_{y'}}\right)^2\right) \end{aligned} \quad (24)$$

$$\begin{aligned} \left(\frac{\Delta D_{PP}}{D_{PP}}\right)^2 &= \left(\frac{\Delta V_r}{V_r}\right)^2 + \frac{1}{4(x\mu_x + y'\mu_{y'})^2} \times \\ &\quad \left((x\mu_x)^2 \left(\frac{\Delta \mu_x}{\mu_x}\right)^2 + (x\mu_x + 2y'\mu_{y'})^2 \left(\frac{\Delta \mu_{y'}}{\mu_{y'}}\right)^2\right) \end{aligned} \quad (25)$$

At large inclination, where $x\mu_x \gg y'\mu_{y'}$, the errors on V_c and D_{PP} simplify to

$$\left(\frac{\Delta V_r}{V_r}\right)^2 + \frac{1}{4} \left(\left(\frac{\Delta \mu_x}{\mu_x}\right)^2 + \left(\frac{\Delta \mu_{y'}}{\mu_{y'}}\right)^2\right).$$

Typical values for proper motions may be $\mu_{x,y'} \sim 16 \mu\text{as yr}^{-1}$ (40 for M31), $\Delta \mu_{x,y'} \sim 4 \mu\text{as yr}^{-1}$, while the radial velocity uncertainty would be less than 10 km s^{-1} . For M31, the fractional errors in the radial velocity and the proper motions equal about, 4%, $\sim 25\%$ and $\sim 10\%$, for V_r , $\mu_{y'}$, and μ_x , respectively. The total fractional errors on D_{PP} , V_c and $D_{y'}$ are of order 15, 15, and 25%, respectively. These values compare well with the exact values presented in Fig. 3.

These considerations indicate that proper motion errors dominate the final uncertainty in the derived distances. The mM distance can have substantially smaller errors. Also note that, in the pure circular motion case, the mM distance estimate requires astrometry for two stars, while the PP distances can be obtained for one star only⁴. We compare the distance

⁴When comparing the final errors on the distances, we multiply the mM errors by $\sqrt{2}$ so as to compare the distance errors per target (i.e. per unit integration time).

error budgets in figures (3)-(9), for M 31, M 33 and M 81 for a range of plausible astrometric errors.

These figures illustrate an important aspect of the single-star method: the attainable distance and inclination errors are not very sensitive to the galactic azimuth θ . As a result, targets from all over the galaxy can be incorporated in the analysis. Furthermore, because of its proximity and large rotation speed, M 31 clearly offers the best opportunity for reliable rotational parallax measurements, followed by M 33 and M 81.

The same figures indicate that the *PP* method works best at low inclinations and that the *mM* method is superior at large inclinations. The latter fact can be understood as follows: for a strongly inclined galaxy, the proper motion perpendicular to the major axis is small ($\mu_M = \mu_{y'} \sim 0$), so that the μ_M term in equation (14) for D_{mM} goes to zero. In that case $D_{mM} \approx |V_{r,M}| / (\kappa\mu_m)$. As a result, the third error-term in equation (22) becomes negligible. For the *PP* method however, both proper motions are required to derive the distance, so that the proper motion error comes in twice.

In figure 10 we present the dependence of the distance errors on both radial velocity and proper motion errors for M 31. In that figure we contour, from top to bottom, the fractional errors on $D_{y'}$, D_{PP} and D_{mM} . For the Local Group galaxies it will pay off to decrease the radial velocity errors to as low values as possible. As expected, proper motion errors dominate the error budget for distant galaxies such as M 81 ($D \sim 3.6$ Mpc, not shown).

Naively, one might expect that of our three distance estimators, $D_{y'}$ would be determined most accurately. After all, for this calculation we *assume* an inclination and we use only *one* proper motion, while D_{mM} and D_{PP} require an additional proper motion measurement. Figure (10) shows that (for $\theta = 30^\circ$) this is not always the case. In fact, the actual expected errors are complex functions of location in the galaxy, inclination, rotation speed and distance. For distant galaxies, the errors are dominated by proper motion errors, so that all three methods are equivalent (not shown). For M 33 all methods yield approximately equally well determined distances, while distance errors for M 31 are minimized if we can use the principal axes method.

For $\Delta\mu_i \sim 1 \mu\text{as yr}^{-1}$ and $\Delta V_r \sim 10 \text{ km s}^{-1}$, the errors on the inferred distance equal about 6, 15, and 10% for M 31, M 33 and M 81, respectively. For the Local Groups galaxies the random motions of stars introduce additional uncertainties. Assuming a dispersion of 10 km s^{-1} , the effective proper motion accuracies are about $2.5 \mu\text{as yr}^{-1}$ at 0.8 Mpc. The internal dispersion at the distance of M 81 is about five times smaller and insignificant with respect to the likely measurement errors that SIM can attain in “reasonable” integration times.

3. Deviations from the Gedanken Galaxy

3.1. Systematic Motions

In section 2.1 we have seen that systematic motions induced by the space motion of the galaxy (\overline{V}_{sys}) can be corrected for rather easily in the principal axes method. Likewise, a global fit to the observed proper motions and radial velocities would allow for the determination of \overline{V}_{sys} in the *PP* method. For example, the radial velocities of M 31, M 33 and M 81 equal -300 ± 4 , -200 ± 6 and -34 ± 4 km s^{-1} . These velocities are comparable to their internal velocities of ~ 270 , ~ 100 and ~ 213 km s^{-1} . We will discuss this issue in later subsections.

3.2. The Effects of Stellar Warps

It is known from radial velocity observations that, for most galaxies, the inclination gradually changes as a function of radius. This so-called “warping” is most pronounced beyond the optical disk (Briggs 1990). Although such inclination changes are hard to detect inside the optical disk, some galaxies are known to warp in the the outskirts of the optical disk⁵, see Reshetnikov & Combes (1998) for a recent review. These authors measured the warps at a distance (R_{25}) where the B-band surface brightness is roughly 25 magnitudes per square arcseconds. This surface brightness is reached at radii of approximately 90 and 31 arc-minutes in M 31 and M 33, respectively (de Vaucouleurs *et al.* 1991).

Cursory inspection of large-scale optical pictures of the Andromeda galaxy suggests that the plane of the galaxy is warped in the outer parts of the galaxy. In fact, the orientation of the outer isophotes starts changing –an indication of a warp– beyond about 90 arc-minutes from the center (Walterbos & Kennicutt 1988).

Also, an analysis of the spiral structure and H I radial velocity field of M 31 suggests that the inclination is about 60° at $10'$ from the center. Due to the almost linear warping of $+0^\circ.3$ per kpc, an inclination of 80° is reached at a radius of $100'$ (Braun 1991). Braun’s determination of the radial inclination gradient is based on the association of H I with spiral arms, but does not self-consistently include the non-axisymmetric velocity component that is likely to be induced by the spiral density wave. It thus may be that the actual warp is less severe than claimed by Braun.

⁵e.g., The Milky Way (Drimmel, Smart & Lattanzi 2000; Porcel, Battaner & Jimenez-Vicente 1997), and references therein, NGC 7814 (Lequeux, Dantel-Fort & Fort 1995), and others (Sanchez-Saavedra, Battaner & Florido 1990; Florido *et al.* 1991)

Similarly, an analysis of the optical spiral arms in M 33 suggests that the inclination of M 33 changes from forty to sixty-three degrees across the disk (Sandage & Humphreys 1980), although this result is disputed (Maucherat *et al.* 1984). On the other hand, the H I warping of M 33 Corbelli & Schneider (1997) sets in around R_{25} (i.e., 30 arcmin, or 8.2 kpc at 0.84 Mpc).

3.3. Spiral Structure

Non-circular orbits, or more generally, streaming motions with respect to the simplified picture of the circular orbit might significantly complicate the determination of rotational parallaxes. Streaming motions induced by spiral density waves can reach tens of kilometers per second, depending on the galaxy, and the locations of the target with respect to the spiral arms. To first order, such deviations would induce systematic errors in the inferred distances that equal the systematic velocities induced by spiral density waves, or about $\Delta V/V_c \sim 20\%$.

The theory of spiral arm density waves has been developed extensively [e.g. (Lin, Yuan & Shu 1969)]. Applications of this theory to radial velocity fields of external galaxies show that streaming motions of the order of 20-50 km s^{-1} [e.g. (Visser 1980; Vogel, Kulkarni & Scoville 1988; Boulanger & Viallefond 1992; Tilanus & Allen 1993)]. The analysis of the spiral structure of M 31 by Braun (1991) indicates streaming motions of 40 km s^{-1} for radii smaller than 40', of 20 km s^{-1} between 30' and 75' and of order 10 km s^{-1} in the outermost parts. M 31 exhibits a well developed two-armed spiral pattern with a small, but radially varying pitch angle Braun (1991). In the inner region, $R \lesssim 27'$, the spiral has a larger pitch angle ($\phi \sim 16^\circ$) than in the outer region ($\phi \sim 7^\circ$).

Stars will respond to the potential induced by the spiral density wave. If the pattern is logarithmic, the radial and tangential velocities [$\tilde{V}_R(R)$ and $\tilde{V}_\theta(R)$] induced by the perturbation can be found analytically. These perturbation velocities vary with (extra) galactocentric radius R . So do the pitch angle and the spiral phase (χ). \tilde{V}_R , \tilde{V}_θ , ϕ and χ can be calculated from the rotation curve, the stellar velocity dispersion, and the pattern-speed and amplitude of the perturbation, where the last three properties are not well established observationally for our target galaxies. This procedure has been followed for the Milky Way (Crézé & Mennessier 1973; Amaral & Lepine 1997; Mishurov et al. 1997; Mishurov & Zenina 1999; Lepine, Mishurov & Dedikov 2000), and can be readily generalized to external galaxies.

It is also possible that the spiral structure is generated in response to a bar or nearby companions. For the Andromeda galaxy, the companions, M 32 and NGC 205, have estimated peri-centers between 13 and 35 kpc [e.g. (Byrd 1976,1977,1978; Sato & Sawa 1986;

Cepa & Beckman 1988)]. In fact, radial velocities and SIM-based proper motions can conceivably be used to *determine* the parameters of the spiral pattern, and allow for detailed tests of various theories of spiral structure.

However, these spiral-structure theories have a large number of parameters. In the density-wave theory, almost all factors that determine the spiral pattern depend on galactocentric radius, so that these “factors” are really *functions* with many more unknowns. Further, on small scales, the details of spiral structure may deviate from the large-scale n -armed spiral. For example, it has been suggested that the large star-formation complex NGC 206 in Andromeda resulted from the recent interaction between two spiral-arm segments, moving with relative velocity of about 30 km s^{-1} (Magnier *et al.* 1997). Alternatively, the often seen bifurcations in the spiral patterns of spiral galaxies may arise from the superposition of spiral modes with different multiplicity. The Milky Way may be an example of two-plus-four armed spiral galaxy (Amaral & Lepine 1997).

Clearly, we would like to avoid the complications that arise due to streaming motions on small and large scales. We will discuss the effects of non-axisymmetric streaming motions in more detail in section 5.

4. Accurate Distances, Notwithstanding Perturbations?

In the previous sections we discussed the case of circular orbits and alluded occasionally to the case of elliptical orbits. A complication of elliptical orbits is that the angle between the orbital velocity and the line-of-sight (θ') can not be deduced from the position of the target and the inclination of the galaxy. That is to say, $\theta' \neq \theta$ [c.f. eqns. (4) and (10)]. This means that predicting the orbital motion (velocity and direction) at point (x_2, y_2) given measurements at (x_1, y_1) becomes significantly more complicated, even if these points lie at the same galactocentric radius. Knowledge of the ellipticity and position angle of the orbit are required to solve this problem. Furthermore, due to the intrinsic dispersions of the target population, additional velocity vectors are added to the motions of the targets. All these parameters are likely to depend on galactocentric distance. And finally, the systemic motion of the galaxy needs to be determined and its effects subtracted from on the individual radial velocities and proper motions.

4.1. $\mu_{y'}$ - V_r Correlations

Here we extend on the procedure to determine the $D_{y'}$ distance [§§ 2.2, eqn. (19)] and make use of the fact that the radial velocity and the $V_{y'}$ velocity are two orthogonal components of the *total* space velocity in the $r - y'$ plane ($V_{tot,ry'}$, see figure 11). Like in equation (19), the distance then follows from the observed radial velocity and y' proper motion: $D_{y'} = V_r / (\kappa \mu_{y'} \tan i_t)$, where i_t is the angle between $V_{tot,ry'}$ and the plane of the sky. Generally speaking, i_t differs from the geometric inclination of the galaxy. For example, i_t will lie between i and 90° if random motions are unimportant and the systemic motion is due to Hubble flow only. We illustrate the various contributions to $V_{tot,ry'}$ in figure 11. From this figure we deduce the following relations for the observed y' proper motion and the radial velocity:

$$V_{y'} = (V_{o,y} + V_{\sigma,y}) \cos i + V_{sys,ry'} \cos i_s + V_{\sigma,z} \sin i \quad (26)$$

$$V_{obs,r} = (V_{c,y} + V_{e,y} + V_{\sigma,y}) \sin i + V_{sys,ry'} \sin i_s - V_{\sigma,z} \cos i \quad (27)$$

where i_s represents the angle between the systemic motion and the plane of the sky. The orbital velocity in the y -direction ($V_{o,y}$) comprises both a circular orbit term ($V_{c,y}$) and a contribution for the ellipticity of the orbit ($V_{e,y}$). The random motions in the y and z directions are denoted as $V_{\sigma,y}$ and $V_{\sigma,z}$, respectively. We now proceed by expressing the observable y' proper motion in terms of the observable radial velocity. To this end we solve eqn. (27) for $(V_{o,y} + V_{\sigma,y})$, substitute the result in (26) and divide by κD to arrive at:

$$\mu_{y'} = \frac{V_{obs,r}}{\kappa D \tan i} + \frac{1}{\kappa D} \left(V_{sys,ry'} \left(\cos i_s - \frac{\sin i_s}{\tan i} \right) + \frac{V_{\sigma,z}}{\sin i} \right) \quad (28)$$

$$= \alpha_{y'} V_{obs,r} + \beta_{y'} . \quad (29)$$

These two equations show that the observable y' proper motion is a linear function of the observable radial velocity. We recognize the $\cos i_s$ and $\sin i_s$ terms in (28) as the y and radial velocity components of the systemic velocity, respectively. More importantly, equation (28) shows that the slope $\alpha_{y'}$ is *independent* of the presence of non-circular motions. This is so because in eqns. (27)-(29) we use the total y component of the orbital speed: for the purpose of distance determination, it is not necessary to know how the total y velocity is distributed between the circular, elliptical and random components.

4.2. μ_x Correlations

Following the method of the previous subsection, we will express the observed μ_x as a function of either the observed radial velocity or the y' proper motion. In order to do so, we need to connect the x and y components of the orbital speed via a simple relation. This is straightforward for the circular component of the orbits. As above, the total observable velocity comprises circular velocities ($V_{c,x}$ and $V_{c,y}$), “elliptical velocities” ($V_{e,x}$ and $V_{e,y}$), random motion components and the systemic velocity. We also employ the r and y' motions derived above [eqns. (26) and (27)] and the x motion:

$$V_{tot,x} = V_{c,x} + V_{e,x} + V_{sys,x} + V_{\sigma,x} \quad (30)$$

First we solve eqn. (27) for $V_{c,x}$, substitute the result in (30) and divide by κD to find μ_x :

$$\mu_{x,r} = -\frac{\tan \theta}{\sin i \kappa D} \Delta V_{obs,r} + \frac{\tan \theta}{\kappa D} \left(V_{e,y} + V_{\sigma,y} - \frac{V_{\sigma,z}}{\tan i} \right) + \frac{V_{e,x} + V_{sys,x} + V_{\sigma,x}}{\kappa D}, \quad (31)$$

where $\Delta V_{obs,r} \equiv V_{obs,r} - V_{sys,r} \sin i_s$. Likewise, when solving the y' proper motion for $V_{c,x}$ and using $\Delta \mu_{y'} \equiv \mu_{y'} - V_{sys,r} \cos i_s$, we find:

$$\mu_{x,y'} = -\frac{\tan \theta}{\cos i} \Delta \mu_{y'} + \frac{\tan \theta}{\kappa D} (V_{e,y} + V_{\sigma,y} + V_{\sigma,z} \tan i) + \frac{V_{e,x} + V_{sys,x} + V_{\sigma,x}}{\kappa D}. \quad (32)$$

In case the orbits are exactly circular, equations (31) and (32) simplify to:

$$\mu_{x,r} = \mu_x = -\frac{y'/x \Delta V_{obs,r}}{\sin i \cos i \kappa D} + \frac{V_{sys,x}}{\kappa D} = \alpha_{x,r} (y'/x \Delta V_{obs,r}) + \beta_x, \quad (33)$$

$$\mu_{x,y'} = \mu_x = -\frac{y'/x \Delta \mu_{y'}}{\cos^2 i} + \frac{V_{sys,x}}{\kappa D} = \alpha_{x,y'} (y'/x \Delta \mu_{y'}) + \beta_{x,y'}, \quad (34)$$

where we have replaced $\tan \theta$ by $y'/(x \cos i)$. The independent variables ($y'/x \Delta V_{obs,r}$) and ($y'/x \Delta \mu_{y'}$) are defined for $x = 0$ since, for circular orbits, they are proportional to $(V_c \sin \theta)$ [cf. eqns. (4)-(9)]. However, the random and elliptical contributions to $\Delta V_{obs,r}$ can “blow-up” close to the minor axis as a result of the multiplication by $1/x$. It is thus advisable to down-weight the regions close to the minor axis. Like the $\alpha_{y'}$ slope derived in the previous subsection, the slope $\alpha_{x,r}$ depends on both the inclination and the distance, but in an independent manner. The correlation between μ_x and $\mu_{y'}$ yields the inclination of the galaxy directly.

The proper motion equations (29), (33), and (34) represent the multi-star equivalent of the single-stars case and include the systemic motion of the galaxy: we solve them for inclination and distance in §4.3 below, and we discuss the effects of non-circular and random motions in section 5.

4.3. The Rotational Parallax Distance

In the previous subsections we found that the y' and x proper motions can be expressed in terms of the observed radial velocities. From these linear slopes the inclination and distance follow:

$$\alpha_{y'} = \frac{1}{\kappa D \tan i} \quad (35)$$

$$\alpha_{x,r} = \frac{-1}{\kappa D \tan i \cos^2 i} \quad (36)$$

$$\cos^2 i = \frac{\alpha_{y'}}{-\alpha_{x,r}} = \frac{1}{-\alpha_{x,yp}} \quad (37)$$

$$D_{\alpha i, xy'} = \frac{1}{\kappa \alpha_{y'} \tan i} \approx \frac{-1}{\kappa \alpha_{x,r} \tan i \cos^2 i} \quad (38)$$

$$D_{\alpha xy'r} = \frac{1}{\kappa \alpha_{y'}} \sqrt{\frac{-\alpha_{y'}}{\alpha_{x,r} + \alpha_{y'}}}. \quad (39)$$

The above relations hold exactly for circular orbits. We will investigate the effects of non-circular orbits in the next subsection. Equations (37) and (38) for i and $D_{\alpha i, xy'}$ are the equivalent of the relations for inclination and distance as derived in the single-star method [(16) and (19)]. It thus follows that $\alpha_{x,r}$ is equivalent to $x\mu_x$, $\alpha_{y'}$ corresponds to $y'\mu_{y'}$ and $\alpha_{y'}\Delta V_{obs,r} \leftrightarrow \mu_{y'}$, so that eqn. (39) is obtained.

4.4. The Systemic Velocity Vector

A straightforward manner to determine the systemic velocity of the galaxy would be to take the appropriate averages of the observed proper motions and radial velocities of targets that have similar $|x|$ and $|y|$ coordinates. In this way, the motions induced by the internal motions of the galaxy are averaged out, so that the components of the systemic velocity of galaxy become apparent. However, due to elliptical streaming motions these values can only be considered to be “reasonable” values. A better determination of the systemic velocity is possible from a full solution of equations (28), (31) and (32).

5. Practical Implementation

In section 3 we have reviewed the various effects that complicate the implementation of the single-star rotational parallax method. Above we outlined the modifications required to measure the systemic motion. In the next subsections we show that neither warping of the stellar disk nor spiral structure inhibits our ability to determine accurate rotational parallaxes.

5.1. Inclination Effects

For many spiral galaxies, it is possible to determine the inclination from the axis-ratio of contours of constant optical surface brightness. For M 31 this procedure is more complicated due to its large inclination and finite thickness. However, the inclination can also be determined from H I velocity fields [e.g., see Unwin (1983) and Brinks & Burton (1984) for M 31 and Corbelli & Schneider (1997) for M 33]. These inclination estimates typically have an uncertainty of a few degrees. If such H I inclination estimates were to be used to determine the distance from the slope of the observed $\mu_{y'}-V_r$ relation, the resulting distance uncertainties would be of order 20% for M 81 and M 33, and a factor of two for M 31. To obtain distance estimates that are accurate at the percent level, the other proper motion component needs to be utilized.

From equations (29), (33), and (34) it is clear that no a-priori knowledge of the inclination is required, *if* the inclination does not vary significantly with radius. In that case, distance and inclination can be determined, even when the targets are arbitrarily located across the face of the galaxy, provided that the kinematic variations are sufficiently sampled. On the other hand, if the inclination does change with radius, it might be best to select targets in an elliptical annulus with an axis-ratio equal to the cosine of the best-guess inclination. The drawback of such an approach is that the range in radii sampled will increase if the a-priori inclination estimate was wrong⁶. In principle, the best distance determination is possible when all targets have similar distances from the galaxy center so as to minimize the effects of any possible radial variations of inclination (and rotation speed).

⁶By about a factor of two for a 2° error at $i_{est} = 75^\circ$.

5.2. Non-Circular Motions

In general, non-circular motions will be present in our target galaxies. The question is, how will those motions affect our ability to determine an accurate rotational parallax. Equations (31)-(34) above show that elliptical motions in both the x and y direction can adversely influence the distance determination. Below we will outline a technique that can be used to detect those motions and correct for their effects.

The contribution from elliptical motions in equations (27) and (30) can be written as the sum of two component. If the angular variation of an elliptical streaming component is identical to the azimuthal dependence of the circular velocity component we term that component “invisible.” That is to say, an invisible elliptical streaming field will induce a proper motion and radial velocity field that is indistinguishable from that of the circular streaming field. Thus, the invisible elliptical motion is given by:

$$\bar{V}_{ei} = V_{ei,x} \sin \theta \hat{x} + V_{ei,y} \cos \theta \hat{y}, \quad (40)$$

with \hat{x} and \hat{y} the unit vectors in the x and y directions, respectively. Also note that, if $V_{ei,x}$ equals $V_{ei,y}$, then the resulting elliptical motion amounts to an additional circular velocity term, and should be absorbed in V_c . All elliptical streaming components orthogonal to \bar{V}_{ei} are directly detectable in the observed stellar motions. The invisible elliptical streaming can significantly bias the inferred inclination and distances since their proper motion and radial velocity signature are indistinguishable from the circular motion terms. In section 5.4 we show how invisible streaming motions can be detected, and their distance-bias corrected for.

The exact functional form of the elliptical streaming field depends on the physical mechanism that drives such non-circular motions (§3.3). A full investigation of the dependence of the effect of non-circular streaming on the accuracy with which the rotational parallax can be determined is beyond the scope of the current work. However, we will explore the effects of non-circular motion by investigating the effects of a toy model for elliptical streaming. This illustrative model has the invisible streaming component discussed above plus an additional orthogonal, visible, component:

$$\bar{V}_{e,toy} = \bar{V}_{ei} + V_{ev,x} \cos \theta \hat{x} + V_{ev,y} \sin \theta \hat{y}, \quad (41)$$

with $V_{ev,x}$ and $V_{ev,y}$ the visible x and y components of the elliptical streaming field, respectively.

5.3. The Works

The rotational parallax distances derived above can be improved upon if the $\mu_{y'}-V_r$ and μ_x-V_r equations [(28) and (33)] are solved simultaneously. In order to arrive at a unbiased solutions in case $\overline{V_{ei}}$ is non-zero, additional constraints are required. For example, one could demand that the inferred radial gradients of the inclination and rotation curve are small and linear. However, better, non-parametric additional constraints are available: 1) the lack of azimuthal variation of the rotation curve inferred from $\mu_{y'}$, V_r and μ_x , and 2) the requirement that the rotation speed derived from these three observable are identical, to within the errors⁷

Such a multiple non-linear regression solution as described above is beyond the scope of the current paper. However, we will investigate a poor-man’s approach to the problem and use that to derive estimates of the accuracy to which the rotational parallax can be determined with an instrument like SIM. Although the multiple regression approach is clearly advisable to make optimal use of the available data, the poor-man’s approach has the advantage that it clearly illustrates the problematic areas of the rotational parallax determination method. Further, since the poor-man’s route will not lead to the best possible solution, the error estimates so obtained are likely to be improved upon when using a multiple non-linear regression technique.

In the poor-man’s approach we split the procedure in four distinct steps. In the first step, the $\mu_{y'}-V_r$ correlation [eqn. (28)] is used to determine a solution for the product of distance and the the tangent of the inclination: $D \times \tan i = (\kappa\alpha_{y'})^{-1}$ [cf. eqn. (38)]. As discussed in section §4.1, this determination of $D \times \tan i$ has no sensitivity to elliptical streaming motions *at all*. In the second step we determine D, i and $\overline{V_{ev}}$ from the μ_x-V_r correlation [eqn. (33)] given the previously determined value for $D \times \tan i$. In the third step, we repeat the previous step N_{try} times. We randomly selected a value for $D \times \tan i$, based on its estimated value and dispersion obtained in step #1. The final best value for the to-be-fitted parameters is obtained by averaging the N_{try} results, where the derived errors equal the second moment of the N_{try} values. In the fourth and final step, we check the additional constraints that the inferred rotation curve should have negligible azimuthal dependence, and that the rotation speed value inferred from the radial velocities and proper motions are equal to within the errors (see the Diagnostics section below for details). In principle, the diagnostics step can already be incorporated in step #2 to improve the estimates on the parameters. We will not do so in the spirit of deriving upper limits to the error budgets.

⁷Since V_r is easier to measure than $\mu_{y'}$ (for M 31), and the resulting $V_c(\theta)$ should be equivalent, we will only use the information contained in V_r and μ_x .

5.3.1. Rotation Speed Diagnostics

Starting from equations (30) and (27) we write⁸:

$$V_{c,x}^{inf}(\theta) \equiv (V_{c,x} + V_{ei,x}) \sin \theta = -[\kappa D \mu_{obs,x} - V_{ev,x}(\theta)] \quad (42)$$

$$V_{c,r}^{inf}(\theta) \equiv (V_{c,r} + V_{ei,y}) \cos \theta = \frac{V_{obs,r}}{\sin i} - V_{ev,y}(\theta), \quad (43)$$

where $V_{c,x}^{inf}(\theta)$ and $V_{c,r}^{inf}(\theta)$ are the circular velocities inferred from the observed x proper motions and the radial velocities, respectively. These equations clearly illustrate that the invisible component of the elliptical streaming motions are indistinguishable from the circular velocity term. Here we retained the general expressions for the visible components of the elliptical streaming field. The right-hand sides (RHSs) of these two equations can be constructed from the observed V_r and μ_x motions and the fitted values for distance, inclination and \bar{V}_{ev} . If the correct values for i and D are used, and if the true visible streaming field is subtracted from the RHSs, equation (42) should show a pure sine modulation, while only the cosine modulation should contain significant power in equation (43).

In general, neither the true inclination and distance, nor the correct elliptical streaming field will be used in the empirical determination of the RHSs of the V_c^{inf} equations. Thus, higher order θ modulations will be observable in the RHSs of the V_c^{inf} equations. The usage of an erroneous inclination (i_e) is most damaging because the estimated position angle, θ_e , is determined from the estimated inclination such that $\theta_e = \arctan(\frac{y'}{x \cos i_e})$. In practice, a search for additional modulations in the V_c^{inf} equations will be performed in terms of the estimated azimuth, not the true azimuth (θ_t). To see what the consequences are, we suppose that the true inclination, i_t , can be expanded to first order around i_e . With $\Delta i \equiv i_e - i_t$ we find:

$$\sin \theta_t \approx \left(1 - \frac{\Delta i}{4} \tan i_e\right) \sin \theta_e - \frac{\Delta i}{4} \tan i_e \sin 3\theta_e \quad (44)$$

$$\cos \theta_t \approx \left(1 + \frac{\Delta i}{4} \tan i_e\right) \cos \theta_e - \frac{\Delta i}{4} \tan i_e \cos 3\theta_e \quad (45)$$

At the inclination of the Andromeda galaxy, the $3\theta_e$ modulations have an amplitude of about $\frac{2\Delta i}{1 \text{ degree}}$ percent of the θ_e amplitudes, or several km s^{-1} . We find that, with a sufficient number targets, such effects are easily detectable.

In fact, if we expand the RHSs of the V_c^{inf} equations in Fourier series, their $3\theta_e$ coefficients can be used to calculate new estimates for the inclination: $\Delta i_c = A_{c3} \frac{4}{\tan i_e}$ and

⁸We set the contributions from the systemic motion and the stellar random velocities to zero.

$\Delta i_s = A_{s3} \frac{4}{\tan i_e}$ with A_{c3} and A_{s3} the measured Fourier coefficients of the $\cos 3\theta_e$, and $\sin 3\theta_e$ modulations. Significant $3\theta_e$ coefficients can occur in two cases: 1) the correct elliptical streaming was determined but the estimated inclination is wrong, and 2) the right inclination was determined, but the wrong $3\theta_e$ components was fitted for the elliptical streaming field. The observed $3\theta_e$ terms can only be used to arrive at a better inclination estimate in case the correct \bar{V}_{ev} has been subtracted. Generally speaking, that can not known to be the case. However, in both cases, the presence of significant $3\theta_e$ terms indicate that the model used is inadequate and that a better solution is possible. Further, the ambiguity of the meaning of any detected $3\theta_e$ modulation also illustrates the necessity of a multiple non-linear regression technique.

5.4. The Invisible Components

So far, the invisible component remains undetectable, even when the $3\theta_e$ constraints are included, and even if a multiple non-linear regression technique has been used. As it turns out, the lowest order (θ_e) Fourier coefficients of the expansion of the V_c^{inf} equations provide powerful additional constraints on the invisible elliptical streaming components.

For example, suppose that \bar{V}_{ei} is non-existent, in that case, the $A_{c\theta}$ and $A_{s\theta}$ coefficients of the cosine and sine modulations should be identical and equal to the rotation speed of the galaxy. If \bar{V}_{ei} is non-zero, $A_{c\theta}$ will not be equal to $A_{s\theta}$. Unfortunately, equations (42) and (43) are not sufficient to determine the three unknowns contained in the two equations. However, it is not necessary to know the values of $V_{ei,x}$ and $V_{ei,y}$ separately. Only the algebraic sum of the two invisible components, $V_{ei,xy}(\theta) \equiv (V_{ei,x} \sin \theta + V_{ei,y} \cos \theta)$, occur in equations (31) and (32). Thus, in these two equations, $V_{ei,xy}(\theta)$ can be replaced by $(A_{s\theta} + A_{c\theta}) - V_c(\sin \theta + \cos \theta)$. In a multiple regression technique, the circular velocity thus becomes a to-be-fitted parameter. As a result, the V_c^{inf} equations will also allow for the determination of both invisible components of the elliptical streaming field.

The arguments presented above show that, with the additional constraint that the V_c^{inf} equations only show a θ modulations, all parameters of the model can be determined. Because even the “invisible” components of the elliptical streaming field can be determined experimentally, the inferred distance, inclination rotation speed and galaxian space motion can be measured without significant systematic errors.

5.5. Final Accuracies

In the SIM book it is suggested one-hundred targets are observed in both M 31 and M 33 and twenty-five in M 81. Our discussion above indicate that systematic errors will be unimportant so that the final attainable distance error is inversely proportional to the square-root of the number of target stars. With such a moderate number of targets and a proper motion uncertainty of $4\mu\text{as yr}^{-1}$, extremely accurate distances can be determined for the nearest spirals: $\Delta D \sim 0.7\%$, 1.9% and 10% ($\times \frac{\Delta\mu}{4\mu\text{as yr}^{-1}}$), for M 31, M 33 and M 81, respectively.

It should be kept in mind that these considerations neglect several important aspects that will be subject of future study. First, systematic effects *internal* to the galaxies such as spiral arm streaming motions or runaway stars will reduce the final achievable results. On the positive side, it will be possible to identify “deviant” objects using the single star method so that they can be eliminated from the target list. Further, it may very well be possible that a global fit to the proper motions and radial velocities of the targets will produce significantly tighter results if we impose smoothness criteria for the radial variation of rotation speed and inclination. It might also be possible to use external information on the radial gradients of the inclination and rotation curve from the H I velocity field to further decrease the errors. This too will be investigated in the near future.

We have generated numerical models that describe the stellar motions in three potential SIM targets: M 31, M 81 and M 3. The stellar disks of these model galaxies are inclined by 77° , 56° , and 57° with respect to the line-of-sight, respectively. The motions of the stars have circular velocity components of 270, 213 and 97.3 km s^{-1} , while we add a random component to the targets of 10 km s^{-1} in all three directions. We computed several models with either fixed inclinations or a small inclination gradient. We also varied the elliptical streaming component, from non-existent to strong (approximately 20% of the circular velocity), where we tried several angular dependencies consistent with the toy model described in section 5.2 (i.e., θ components only). Our method of analysis of this model data is described by the poor-man’s approach of section 5.3. We ran six different models with 100-600 targets. Each of these models were “observed” $N_{try} = 200$ times where for each try we added random terms to the stellar space motions to simulate observational errors. To the radial velocity we added random errors from 2.5 to 10 km s^{-1} , in steps of 2.5 km s^{-1} , while we used a large range of proper motion errors (between 1 and $50 \mu\text{as yr}^{-1}$).

The results for the three galaxies are summarized in figures 13-15. Each of these three figures contain three rows and four columns. The results for the smallest number of targets are displayed in the top row, those for the largest number of stars in the bottom panels. In the left two columns we plot the inferred rms and systematic distance errors, respectively.

The two systemic error flags (SEFs) are plotted in the two right columns. For M 31, for which the observed proper motions are largest, the rms errors are encouragingly small, even for a small number of targets. The inferred systematic errors are also small, which is confirmed by the small SEF values. For the other two galaxies, significant systematic errors result from the poor-man’s approach. This is probably a result of the fact that these galaxies have smaller rotational proper motions. On the positive side, the SEFs are also clearly raised, indicating that the poor-man’s solutions are erroneous.

5.6. Beyond SIM

If the systemic velocity is zero, the systematic variation of of the distance D^9 along an annulus will introduce a deviation from the linear behavior of eqn. (29). However, the deviation due to the “proximity effect”, $\Delta\mu_{y'}$, is rather small: $\Delta\mu_{y'} \sim 4, \sim 0.14, \sim 0.09$ and ~ 0.01 mas yr⁻¹ for the LMC, M 31, M 33 and M 81, respectively. The constant $\beta_{y'}$ in eqn. (29) has a distance dependence as well so that the systemic velocity terms will also contribute to $\Delta\mu_{y'}$. In fact, because the contribution to $\Delta\mu_{y'}$ from internal motions is down-weighted by the $1/\tan i$ term, the systemic contribution to $\Delta\mu_{y'}$ tends to outweigh the former. However, for “reasonable” values of the systemic velocity, $\Delta\mu_{y'}$ will be still be rather small.

With the possible exception of the Magellanic Clouds, we do not expect that it will be possible to determine the proximity effect with SIM data, in part due to the small number of stars that SIM can measure. Recall that a velocity dispersion of 10 km s⁻¹ corresponds to about 3 mas yr⁻¹, or about twenty times the proximity effect, at the distance of M 31. Assuming that measuring $\Delta\mu_{y'}$ at ten V_r positions would suffice to determine the proximity effect, we estimate that at least $10 \times 20^2 = 4000$ targets are required. This would take about 6,000 hours or about 20% of the science time available during the SIM mission.

⁹ $D(R, \theta) = \sqrt{[D(R=0) + R \sin \theta \sin i]^2 + [R \cos \theta]^2}$

REFERENCES

- Amaral L.H. & Lepine J.R.D., 1997, MNRAS, 286, 885
- Boulanger F. & Viallefond F., 1992, A&A, 266, 37
- Braun R., 1991, ApJ, 372, 54
- Brinks E. & Burton W.B., 1984, A&A, 141, 195
- Briggs F.H., 1990, ApJ, 352, 15
- Byrd G.G., 1978, ApJ, 226, 70
- Byrd G.G., 1977, ApJ, 218, 86
- Byrd G.G., 1976, ApJ, 208, 688
-
- Cepa J., Beckman J.E., 1988, A&A, 200,21
- Crézé, M., Mennessier, M.O., 1973, A&A, 27, 281
- Corbelli E. & Schneider S.E., 1997, ApJ, 479, 244
- de Vaucouleurs G. *et al.*, 1991, Volume 1-3, XII, Springer-Verlag, Berlin, Heidelberg, New York
- Drimmel R., Smart R.L. & Lattanzi M.G., 2000, A&A, 354, 67
- Florido E. *et al.*, 1991, A&A, 242, 301
- Lepine J.R.D., Mishurov Yu.N., Dedikov S.Yu, 2000, astro-ph/0001216
- Lequeux J., Dantel-Fort M. & Fort B., 1995, A&A, 296, L13
- Lin, C.C., Yuan, C., Shu, F.H., 1969, ApJ, 155, 721
- Magnier E.A., Prins S., Augusteijn T., van Paradijs J., Lewin W.H.G., 1997, ApJ, 326, 442
- Maucherat A.J., Figon P., Dubout-Crillon R. & Monnet G., 1984, A&A, 133, 341
- Mishurov, Yu. N., Zenina, I.A., 1999, A&A, 341, 81

- Mishurov Y.N., Zenina I.A., Dambis A.K., Mel’Nik A.M. & Rastorguev A.S., 1997, *A&A*, 323, 775
- Porcel C., Battaner E. & Jimenez-Vicente J., 1997, *A&A*, 322, 103
- Reshetnikov V. & Combes F., 1998, *A&A*, 337, 9
- Sanchez-Saavedra M.L., Battaner E. & Florido E., 1990, *MNRAS*, 246, 458
- Sandage A. & Humphreys R.M., 1980, *ApJ*, 236, L1
- Sato N.R. & Sawa T., 1986, *PASJ*, 38, 63
- The SIM book, 1999 <http://sim.jpl.nasa.gov/library/book.html>
- Tilanus R.P.J. & Allen R.J., 1993, *A&A*, 274, 707
- Unwin S.C., 1983, *MNRAS*, 205, 773
- Visser H.C.D., 1980, *A&A*, 88, 159
- Vogel S.N., Kulkarni S.R. & Scoville N.Z., 1988, *Nature*, 334, 402
- Walterbos R.A.M. & Kennicutt R.C. Jr., 1988, *A&A*, 198, 61

Face-on View of Any Observing Geometry

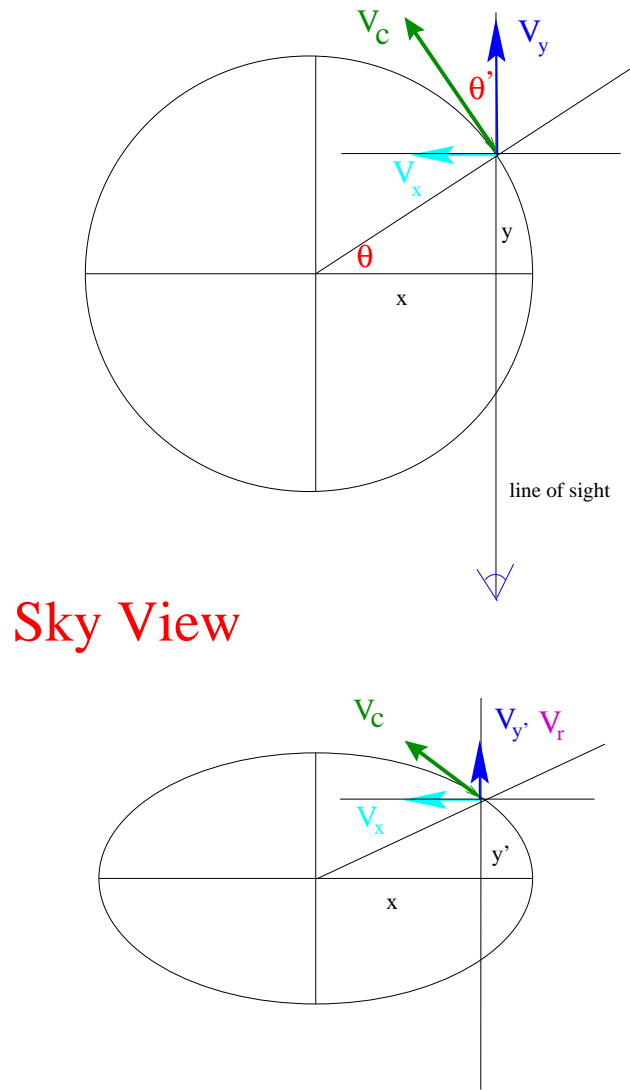


Fig. 1.— The face-on view (top panel) of a galaxy that is observed at an arbitrary inclination (lower panel). The coordinate system (x, y, y', θ) , the line-of-sight, as well as the components of the circular velocity (V_c) are indicated. Note that the angles θ and θ' are identical if orbit is circular.

Sideways View

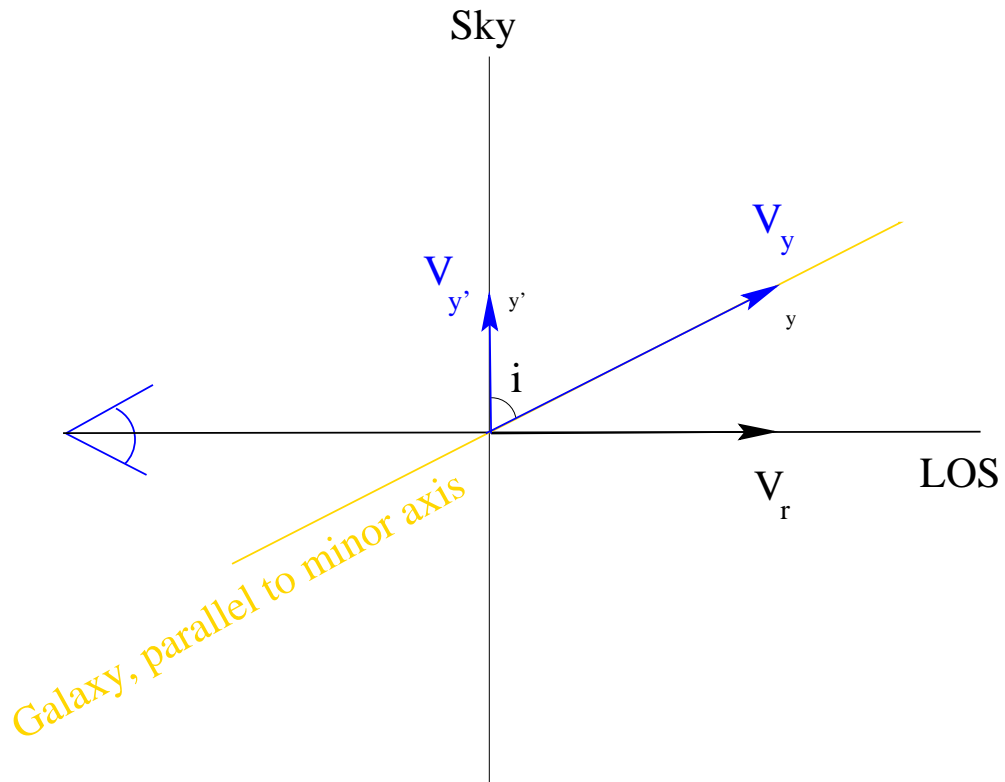


Fig. 2.— The side-on view of a galaxy that is observed at intermediate inclination. The x -axis points out of the paper, the z -axis lies in the $r - y'$ plane, perpendicular to the y axis.

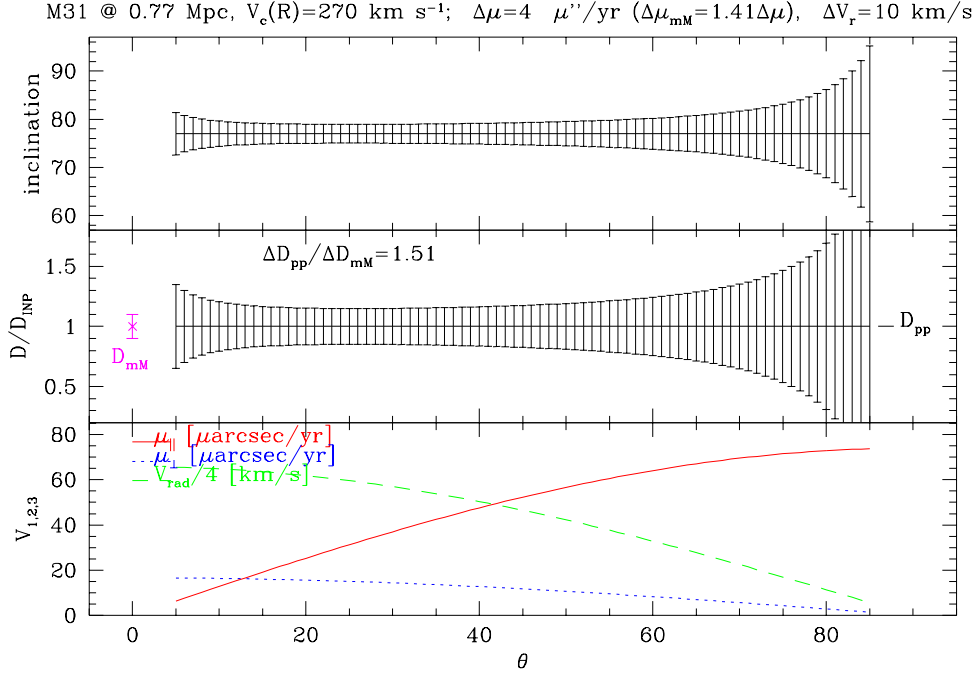


Fig. 3.— Rotational parallax considerations for M31 with $4 \mu\text{as yr}^{-1}$ astrometry errors. Inferred inclination (top panel) and distances (middle panel) from the observable proper motions and radial velocity (bottom panel). All parameters as a function of galactic azimuth θ ($=0.0$ at the major axis, $=90$ at the minor axis). The model input parameters are listed above the figures. The inclination was calculated from eqn. (16). In the middle panel we plot the principal axes distance [D_{mM} ; eqn. (14)] at $\theta = 0^\circ$, and the distances derived from the proper motion parallel to the minor axis [D_{PP} ; eqn. (20)]. The ratio of the PP and mM errors indicated in the middle panel corresponds to the *smallest* ΔD_{PP} value, at $\theta \sim 25^\circ$

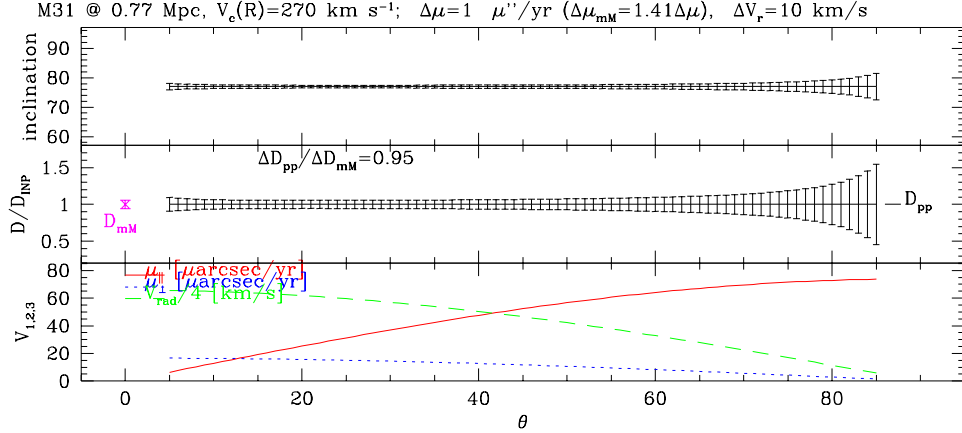


Fig. 4.— Rotational parallax considerations for M31 with $1 \mu\text{as yr}^{-1}$ astrometry errors. Caption as in fig. 3.

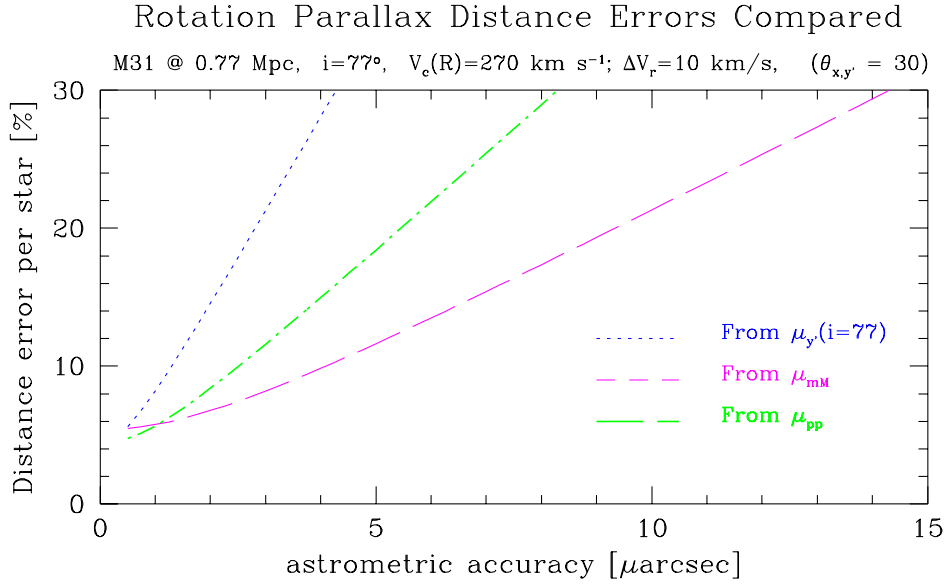


Fig. 5.— Inferred distance errors for M31 as a function of measurement errors. For three different estimates of D . The magnitude of the smallest distance error, at $\Delta\mu = 0.5 \mu\text{as yr}^{-1}$, is set by the assumed radial velocity error.

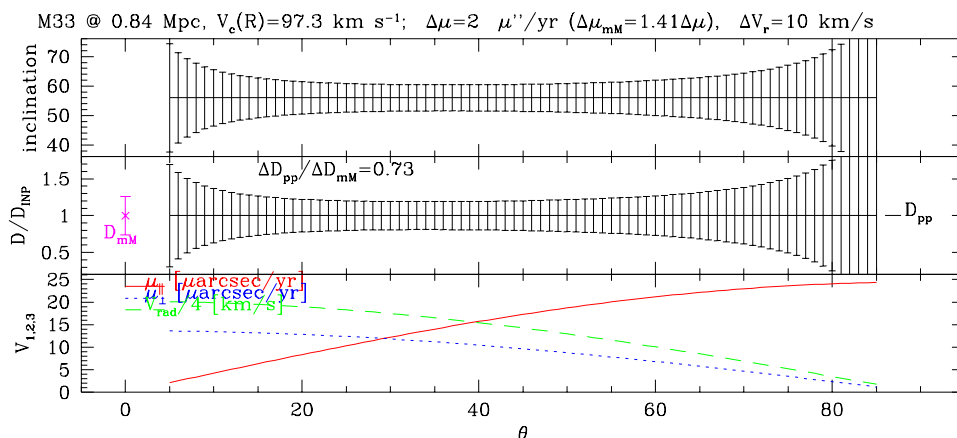


Fig. 6.— Rotational parallax results for M33 with $2 \mu\text{as yr}^{-1}$ astrometry errors. Caption as in fig. 3

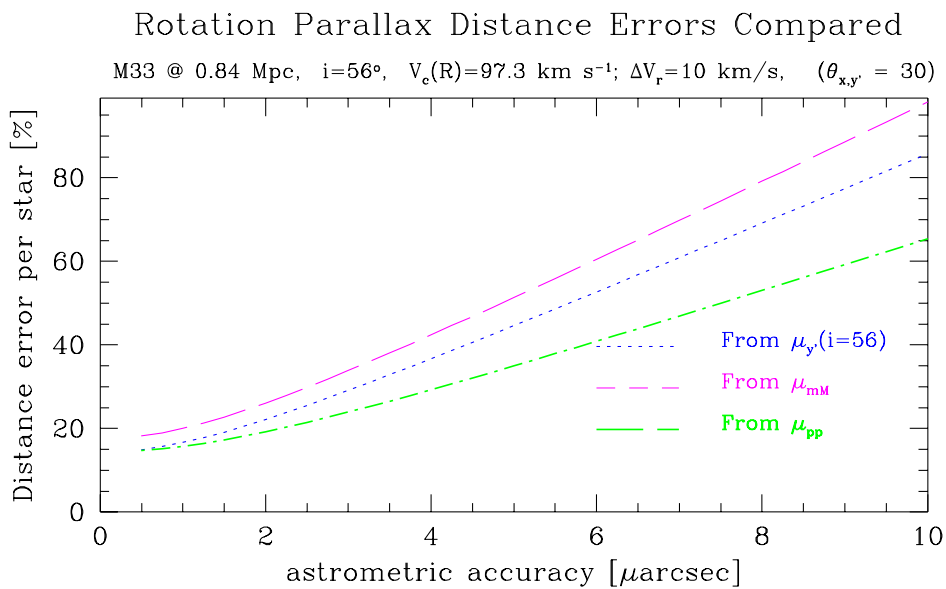


Fig. 7.— Inferred distance errors for M33 as a function of measurement errors. Caption as in fig. 5.

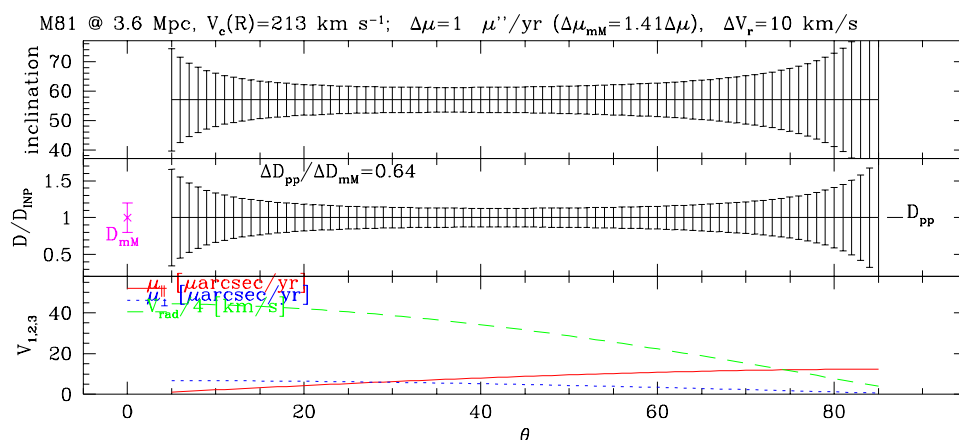


Fig. 8.— Rotational parallax results for M81 with $1 \mu\text{as yr}^{-1}$ astrometry errors. Caption as in fig. 3.

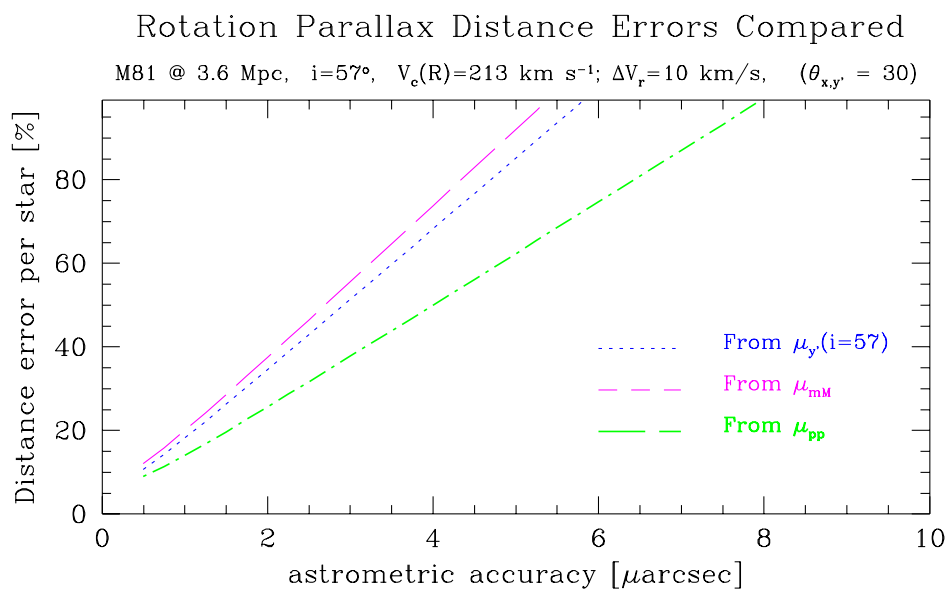


Fig. 9.— Inferred distance errors for M81 as a function of measurement errors. Caption as in fig. 5.

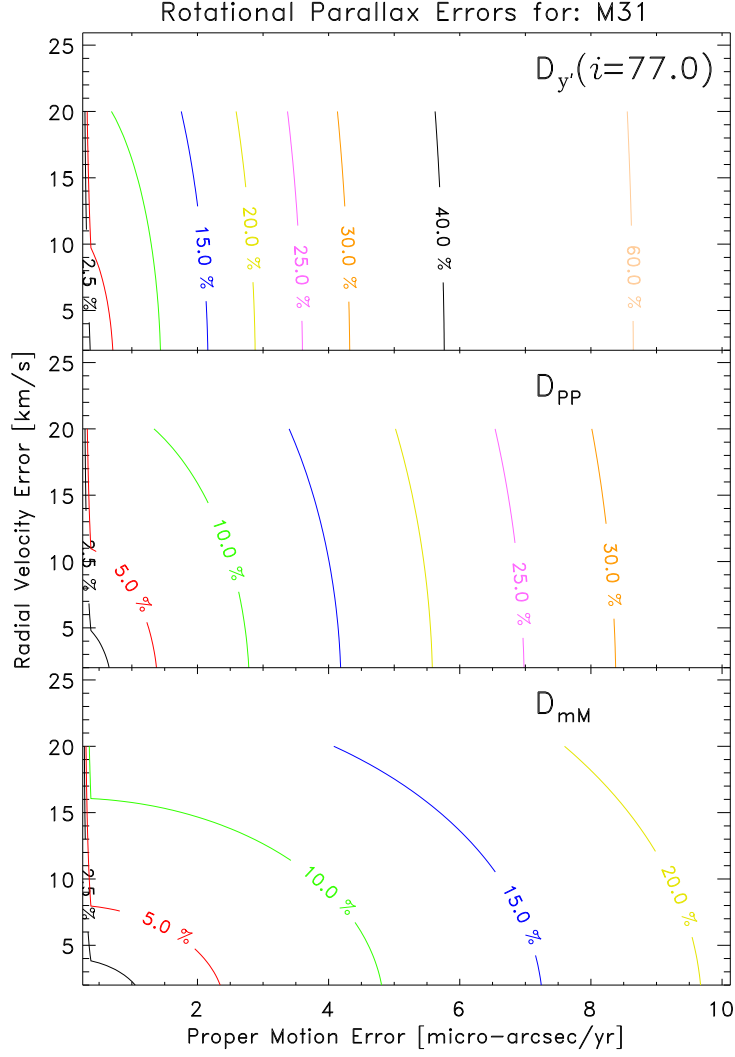


Fig. 10.— Rotational parallax errors for M 31 as a function of the astrometry errors (horizontal scale) and the radial velocity errors (vertical scale). In the top panel we plot the distance as inferred for a *single star* from its radial velocity and proper motion perpendicular to the galaxy’s major axis ($D_{y'}$) as given by eqn.(21). In the middle and bottom panels we plot the *PP* and *mM* distance errors, respectively [cf. eqns. (25) and (22)]. The D_{PP} and $D_{y'}$ distances were calculated for a representative (fig. 3) galactocentric azimuth of $\theta = 30^\circ$.

Sideways View, Systemic Motions

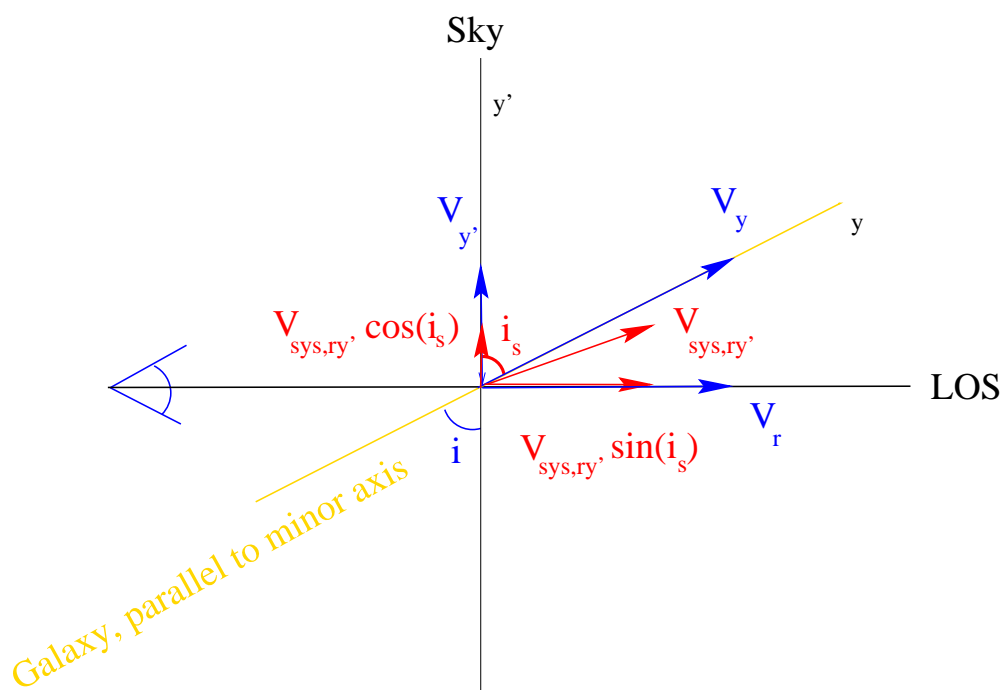


Fig. 11.— The side-on view of a galaxy that is observed at intermediate inclination. In addition to the components resulting from circular motions as in fig. (2) we include (the observable projections of) three other components: 1) the systemic velocity in the $r - y'$ plane ($V_{sys,ry'}$, red), 2) a contribution from the ellipticity of the orbit ($V_{e,y}$), 3) a random motion term in the plane of the galaxy ($V_{\sigma,y}$) and 4) the random motion component out of the plane ($V_{\sigma,z}$). The systemic motion $V_{sys,ry'}$ is inclined by i_s degrees with respect to the plane of the sky. The total ry' velocity equals the vector sum of orbital, systematic and random motion terms, and is inclined by i_t degrees with respect to the plane of the sky.

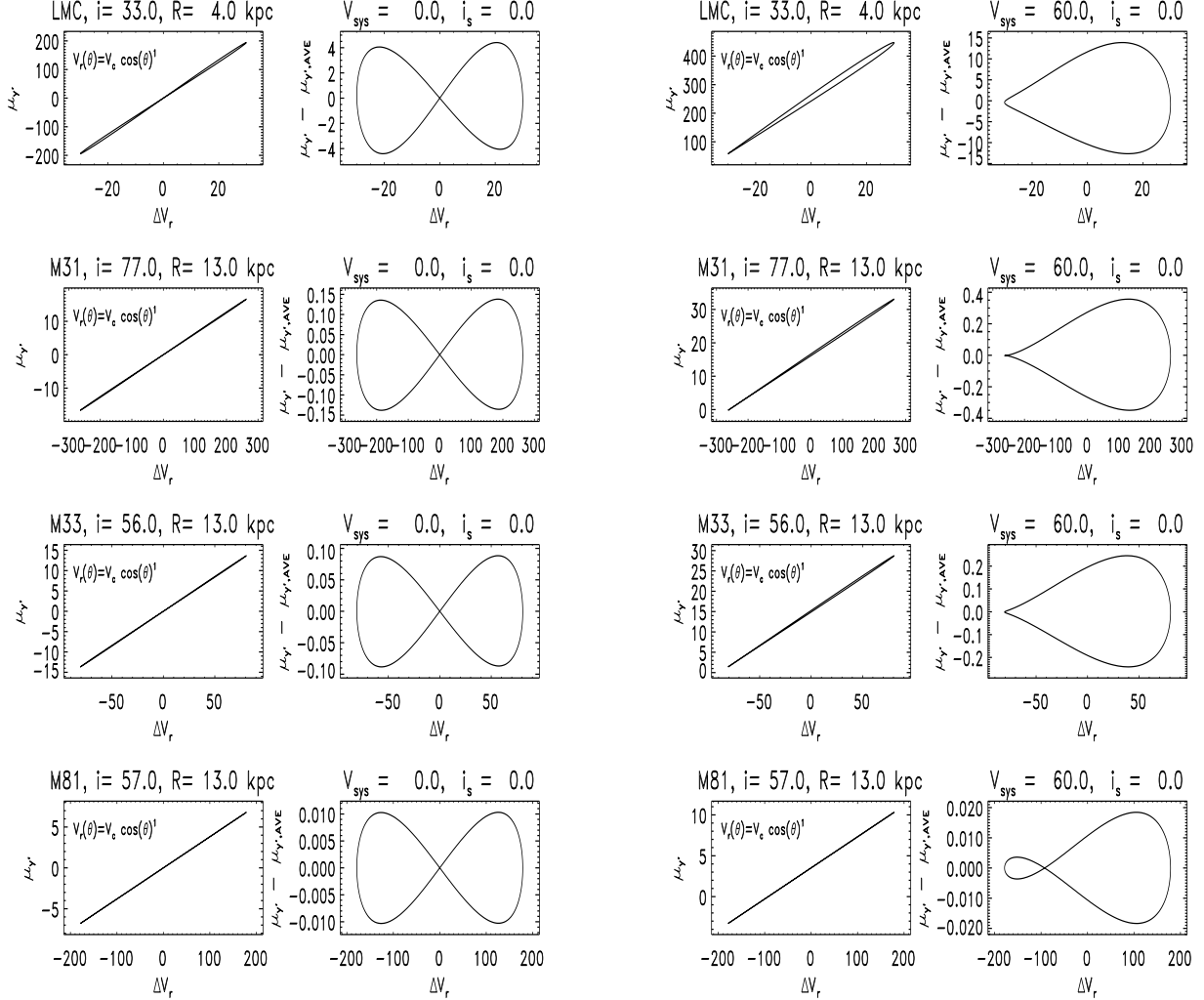


Fig. 12.— The proper motion $\mu_{y'}$ as a function of $\Delta V_r [\equiv V_r - V_{r,\text{sys}}]$ calculated according to eqn. (28). The orbital velocities are based on circular motion along a ring of radius 13 kpc: $V_r = V_c \cos \theta$. We present two sets of panels: in the left hand set the systemic motion of the galaxies is set to zero, the right hand set was calculated for $V_{\text{sys},y'} = 60 \text{ km s}^{-1}$. In each panel, we plot two columns. In the left column we plot $\mu_{y'}$ as a function of ΔV_r , in the right figures we have subtracted the average regression. The four rows are, from top to bottom, the LMC ($V_c = 55$), M 31 ($V_c = 270$), M 33 ($V_c = 97.3$), M 81 ($V_c = 213$) simulated at the inclination indicated. As predicted by eqn.(28), the regression line is straight and $D \times \tan i$ can be determined. The deviation from the regression line allows, in principle, to determine the distance to the galaxy. However, the amplitude will be too small for a reliable SIM determination, except possibly for the LMC.

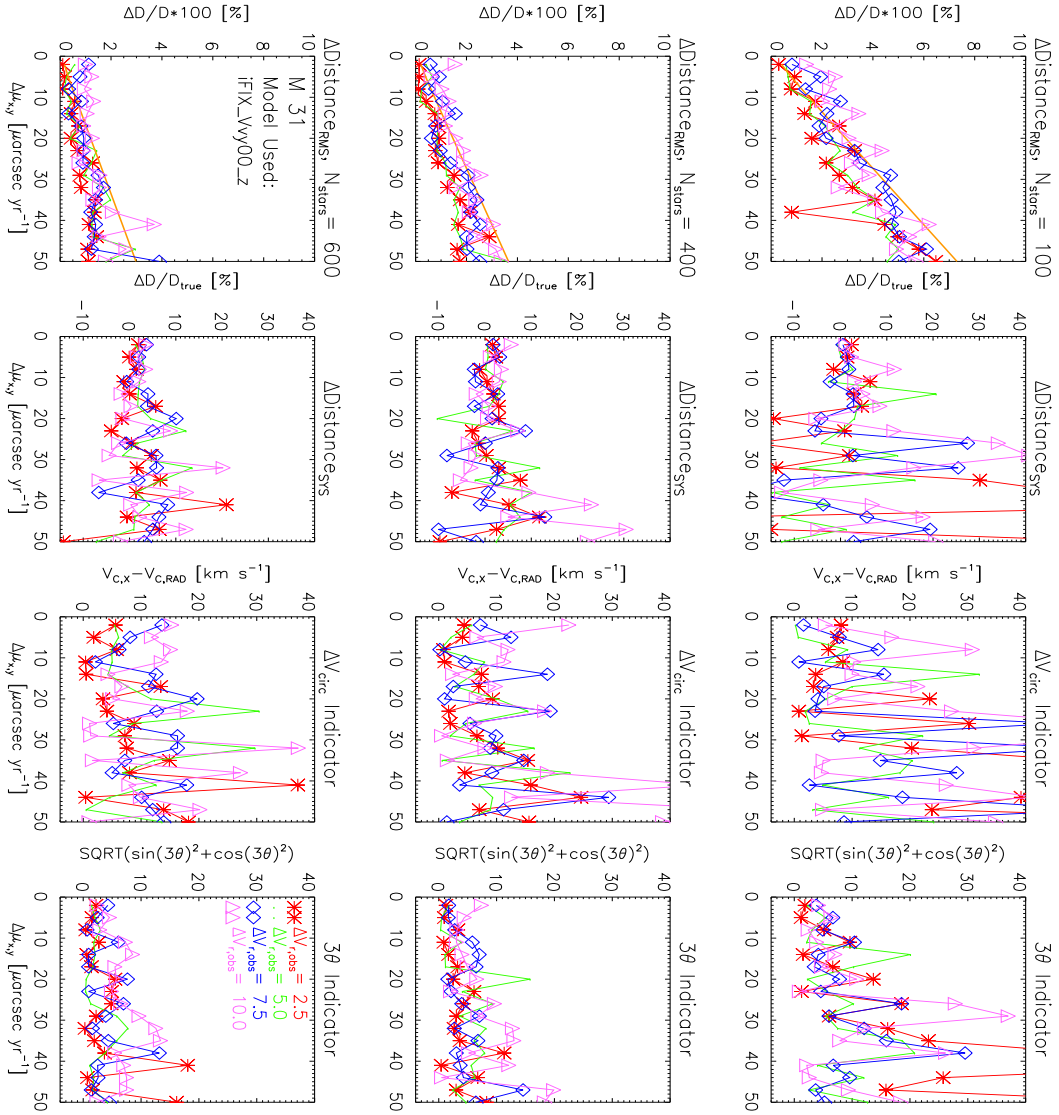


Fig. 13.— The results of “measurements” of simulated M 31 models (see §5.5 for details). The results for 100, 400 and 600 targets are displayed in the top, middle and bottom rows. In the left two columns we plot the rms and systematic distance errors, respectively. The two systemic error indicators are plotted in the two right columns. In each panel, four cases are plotted with observational errors between 2.5 and 10 km s^{-1} . In the “RMS” error plot, we also draw a line (thick, orange) derived from the mM error formula [eqn. (22)] with N_{stars} targets.

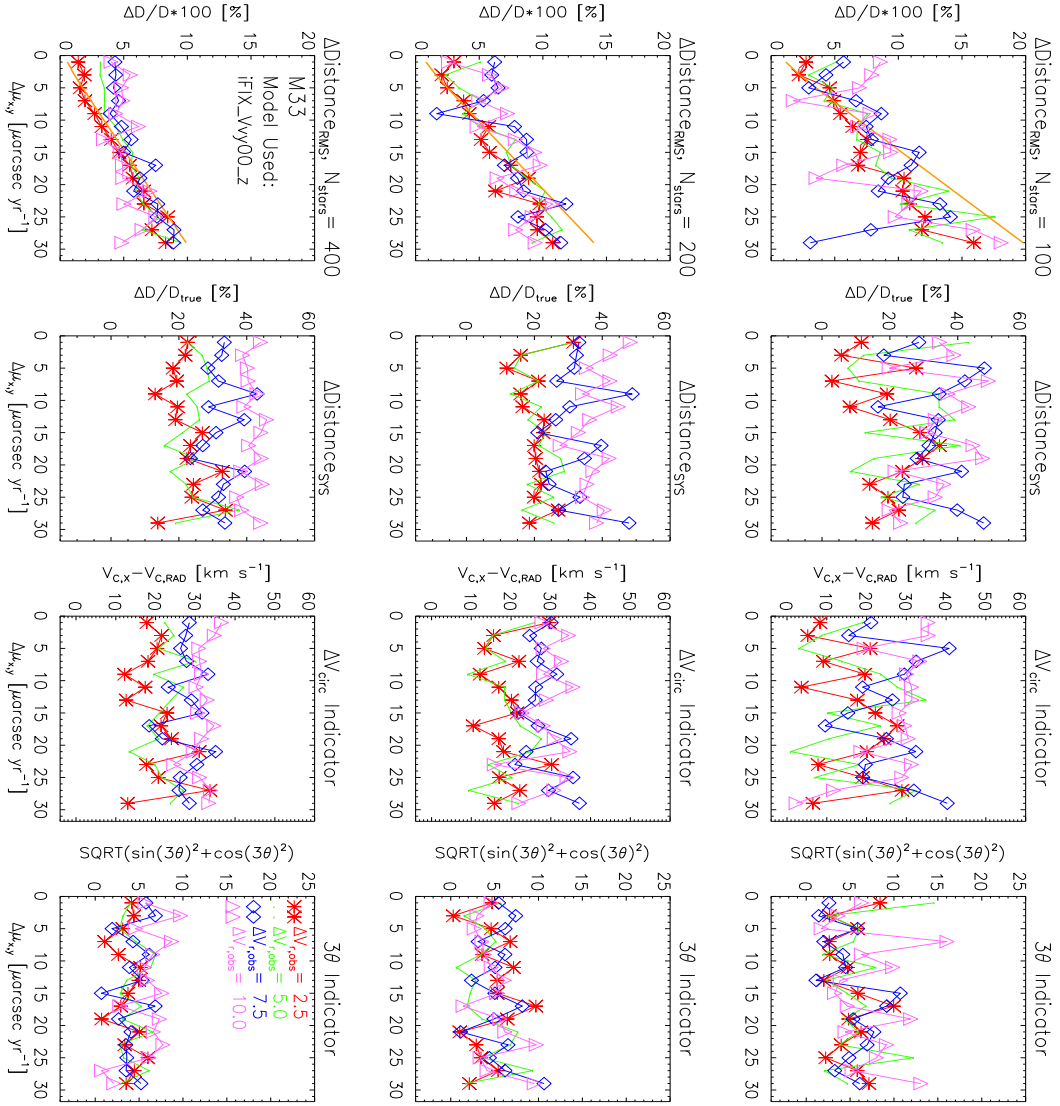


Fig. 14.— Same as for figure 13, but for M 33. The number of simulated targets equals, 100, 200 and 400, from top to bottom.

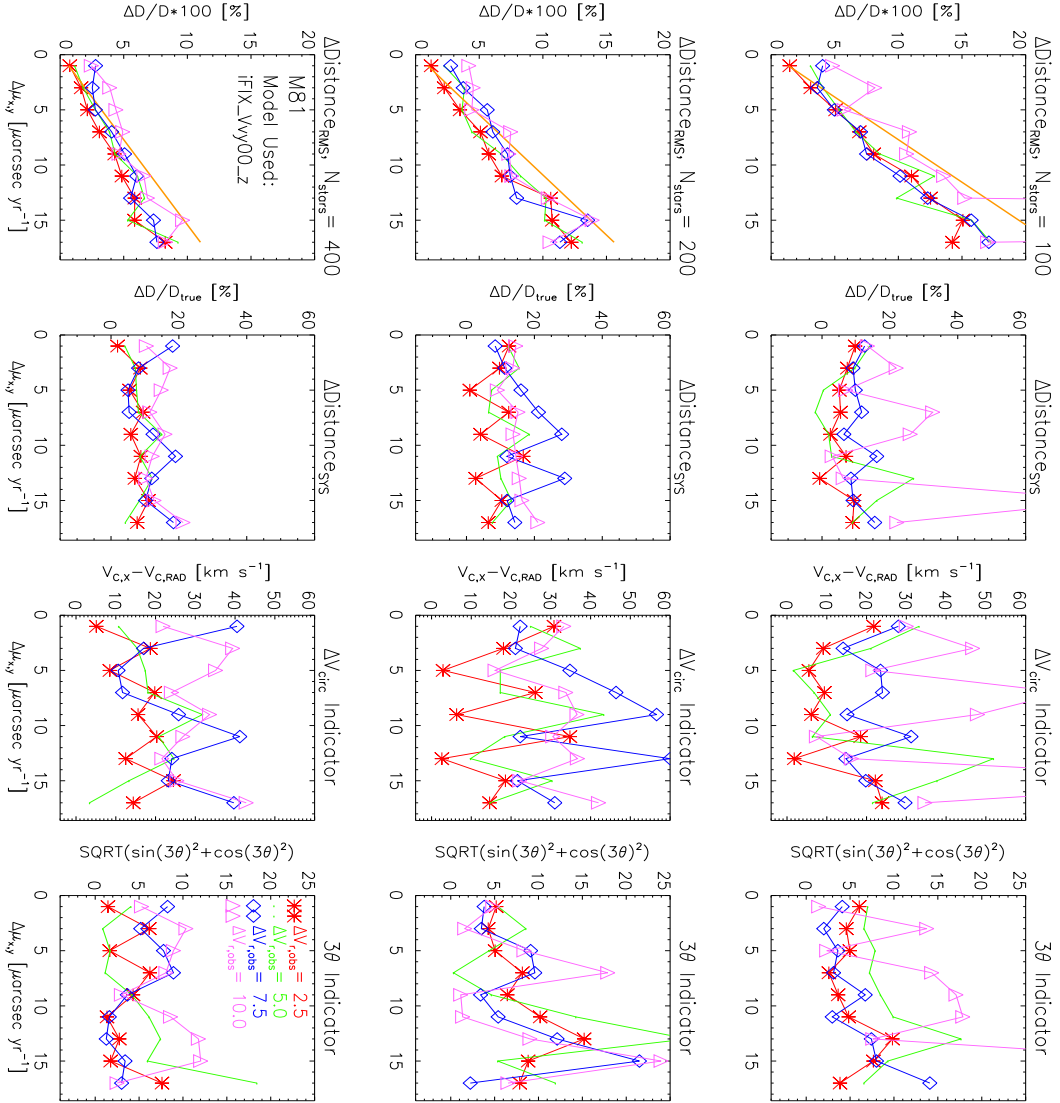


Fig. 15.— Same as for figure 13, but for M 81. The number of targets is as for M 33.